Fermi surface reconstruction under pressure in the kagome metal CsV₃Sb₅

Cole Phillips [1,*] Kyryl Shtefiienko [1,*] Thinh Nguyen [1] Andrea N. Capa Salinas [2] Birendra A. Magar [3]
Ganesh Pokharel,[2,4] Stephen D. Wilson [2] David E. Graf,[5,6] and Keshav Shrestha [1,†]

[1]*Department of Chemistry and Physics, West Texas A&M University, Canyon, Texas 79016, USA*
[2]*Materials Department, University of California, Santa Barbara, California 93106, USA*
[3]*Department of Physics, New Mexico State University, Las Cruces, New Mexico 88003, USA*
[4]*Perry College of Mathematics, Computing, and Sciences, University of West Georgia, Carrollton, Georgia 30118, USA*
[5]*Department of Physics, Florida State University, Tallahassee, Florida 32306, USA*
[6]*National High Magnetic Field Laboratory, Tallahassee, Florida 32310, USA*

This work presents the evolution of the electronic properties of kagome superconductor CsV₃Sb₅ under pressure. The magnetoresistance under high fields of 43 T showed clear Shubnikov–de Haas (SdH) oscillations with multiple frequencies up to 2000 T. With the application of pressure, we observed a sudden change in SdH oscillations with the disappearance of the high-frequency signal near the critical pressure $P_{c1} \sim 0.7$ GPa. We argue that this change could be due to a reconstruction of the Fermi surface (FS) in CsV₃Sb₅. To interpret our experimental data, we computed the electronic band structures and FS of CsV₃Sb₅ using *ab initio* density functional theory. Our results indicate that both the electronic bands and FS of CsV₃Sb₅ are highly sensitive to external pressure. The deformation of FS pockets with increasing pressure qualitatively explains our experimental observations. The pressure-driven FS instability in CsV₃Sb₅ may induce changes in its electronic states, such as superconductivity, charge density wave, nontrivial topology, and more. Therefore, these results are invaluable for gaining insights into these electronic states in CsV₃Sb₅, as well as in other kagome materials.

I. INTRODUCTION

The recent discovery of kagome materials has attracted significant attention as they host several emergent quantum phenomena, such as superconductivity (SC), charge density wave (CDW), nontrivial topology, and geometrically frustrated magnetism [1–4]. A new vanadium-based family, AV₃Sb₅ (A = K, Rb, and Cs), which forms a corner-sharing hexagonal kagome lattice of V atoms [Fig. 1(a)], exhibits SC (T_c = 0.3–3 K) and the CDW phase below $T^* \sim$ (80–110 K) [5–7]. Electronic band structure studies using the density functional theory (DFT) have revealed that AV₃Sb₅ possesses several Dirac points, Van Hove singularities near the Fermi level, and exhibits nonzero $\mathbb{Z}_2$ topological invariants [4,8,9]. The transition to the CDW phase of AV₃Sb₅ leads to the formation of a 2×2 superlattice in the in-plane direction [10]. However, discrepancies exist in the out-of-plane direction, with reports of either doubling [11,12] or quadrupling [13,14] of the unit cell. The doubling or quadrupling of the lattice in the CDW phase leads to the renormalization of electronic bands and to Fermi surface (FS) reconstruction in AV₃Sb₅. Recently, we reported the FS properties of AV₃Sb₅ using high-field torque magnetometry and tunnel diode oscillator (TDO) experiments [15–17], along with other research

groups [14,18–25]. Our findings also confirmed their nontrivial topology.

The effect of pressure (P) in CsV₃Sb₅ is quite intriguing. While increasing P, the CDW order is gradually suppressed, and it disappears completely at 2 GPa; however, SC shows an M-shaped double-dome feature [26,27]. First, T_c increases, reaching a maximum at $P_{c1} \sim 0.7$ GPa, then decreases up to 1.25 GPa, and rises again, showing another maximum T_c at $P_{c2} \sim 2$ GPa. The critical field (H_c) also exhibits the double-dome feature with pressure showing maximum values at P_{c1} and P_{c2}. The emergence of a new stripelike CDW state is reported between P_{c1} and P_{c2} in recent nuclear magnetic resonance (NMR) experiment [28]. The suppression of the CDW phase and the double-dome SC feature has also been observed in doping studies [29–32]. The scanning tunneling microscopy (STM) experiment [31] exhibits two distinct SC pairing symmetries that exist in these domes. As both SC and CDW originate from the FS instability, their change at P_{c1} strongly suggests that the FS has undergone reconstruction under pressure.

Furthermore, recent x-ray diffraction (XRD) and DFT studies [33,34] in CsV₃Sb₅ have shown a strongly anisotropic pressure effect on lattice parameters. As a result, Sb atoms are pushed closer together, forming strong covalent bonds between them. This ultimately leads to a concurrent reconstruction of the FS in this compound. While there are several FS studies of AV₃Sb₅ at ambient pressure [14–25], reports under high physical pressure remain scarce. There are mainly three ways to probe the FS of metals: angle-resolved
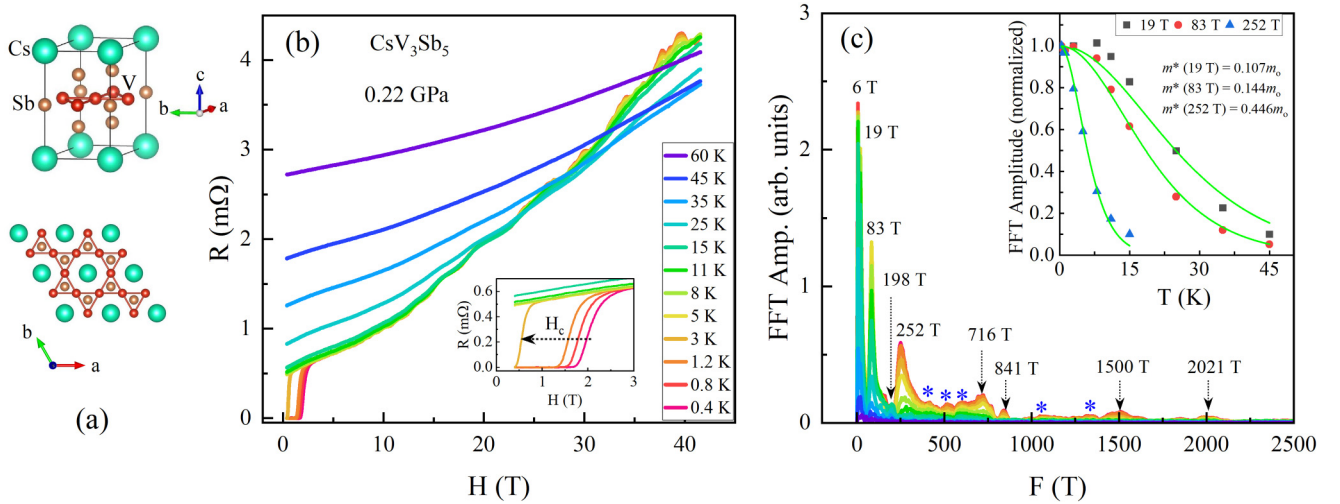

205135-1

FIG. 1. (a) Unit cell of CsV_3Sb_5 (top panel) and kagome layer of V atoms (bottom panel). (b) Magnetoresistance (MR) data of CsV_3Sb_5 at different temperatures measured at $P = 0.22$ GPa. In the low-field region, MR shows a superconductivity feature at low temperatures. MR shows quantum oscillations above 10 T. Inset: The resistance vs H plot at the low-field region. The critical field H_c decreases at higher temperatures, as indicated by the dashed arrow. (c) The frequency spectrum for SdH oscillations shown in (b). There are nine distinct peaks up to 2021 T. Some unknown frequency peaks are indicated by asterisks. Inset: Lifshitz-Kosevich (LK) analyses for frequencies at 19, 83, and 252 T.

photoemission spectroscopy (ARPES), STM, and quantum oscillation measurements. However, the former two methods are not suitable for conducting experiments under high pressure. In this study, we conducted *in situ* magnetotransport measurements under high magnetic fields and pressure to investigate the fermiology of CsV_3Sb_5. Our results indicate that the high-frequency signal in quantum oscillations disappears above P_{c1}, strongly suggesting a reconstruction of the FS at this pressure. Electronic structures calculated using DFT also support our experimental observation.

II. EXPERIMENTAL AND COMPUTATIONAL DETAILS

Single crystals of CsV_3Sb_5 were synthesized from Cs (liquid, 99.98%), V (powder, 99.9%), and Sb (shot, 99.999%) using a flux-based growth technique. Vanadium powder purchased from Sigma-Aldrich was further purified using a mixture of hydrochloric acid and ethanol to remove residual oxides. All further preparation for the synthesis of CsV_3Sb_5 was performed in an argon-filled glove box due to the extreme reactivity of elemental Cs. Elemental reagents of Cs, V, and Sb with stoichiometry of 20:15:120 were milled in a preseasoned tungsten carbide vial for about an hour. The milled powder was loaded into an alumina crucible and then sealed inside a stainless steel tube. The samples were heated to 1000 °C at 200 °C/hr and kept there for 10 h. Then the samples were subsequently cooled to 900 °C at 50 °C/hr and then to 500 °C at 2 °C/hr. Once cooled, the grown platelike single crystals were manually separated from the flux. The residual resistivity ratio (RRR), defined as R(300 K)/R(4 K), was approximately 66, indicating high crystal quality, as presented in Fig. S1 in the Supplemental Material (SM) [35]. The temperature-dependent electrical resistance exhibits a clear charge density wave (CDW) transition at 94 K and a superconducting critical temperature (T_c) of 2.8 K. The magnetic susceptibility also

shows clear anomalies at 2.8 and 94 K, arising from the superconducting and CDW transitions, respectively (Fig. S2 in SM [35]). These values for RRR, T_c, and the CDW transition temperature are consistent with previously published results [5,15].

Magnetotransport measurements under pressure were conducted at the National High Magnetic Field Laboratory (NHMFL) in Tallahassee, Florida, using both hybrid (maximum field 43 T) and resistive (maximum field 41.5 T) magnets, along with a top-loading ^{3}He cryostat. The experimental data presented here are a combination of results obtained from two independent high-quality samples of CsV_3Sb_5, measured in both a hybrid magnet (43 T) and a resistive magnet (41.5 T) at NHMFL. A shiny piece of CsV_3Sb_5 was carefully selected, and four gold wires were attached using silver epoxy for standard four-probe resistance measurements. We generated hydrostatic pressure conditions using a piston-cylinder pressure cell. Daphne 7474 oil was used as the pressure-transmitting medium, and the pressure inside the cell at low temperatures was calibrated by measuring the fluorescence of a small ruby chip mounted inside the cell. The current was applied along the *ab* plane of the crystal. The sample platform was positioned inside the pressure cell such that the magnetic field was directed nearly along the *c* axis of the sample (i.e., $H \parallel c$ axis).

We have performed structure relaxation of CsV_3Sb_5 at different pressure points using an open-source code, QUANTUM ESPRESSO [36]. We allowed variation of both the atomic positions and lattice constants (vc-relax) and then utilized the optimized structures to calculate the electronic properties of CsV_3Sb_5. The electronic bands and FS properties were computed by DFT-based calculations using the full-potential linearized augmented plane-wave (FP-LAPW) method as implemented in the WIEN2K code [37]. The exchange and correlation energy was considered in the Perdew-Burke-Ernzerhof

Generalized Gradient Approximation (PBE-GGA) [38]. The energy convergence criteria was set to 10^{-4} Rydberg for the self-consistent calculation. The atomic sphere radii Radius Muffin-Tin were 2.50, 2.41, and 2.50 Bohr for Cs, V, and Sb, respectively. The self-consistent calculations were performed by taking a set of 500 k points within the full Brillouin zone. Similarly, denser k points of 3000 were used for calculating the FS at different pressure values.

III. EXPERIMENTAL RESULTS

Figure 1(b) shows the MR plots for CsV_3Sb_5 at different temperatures and under the applied pressure of 0.22 GPa. In the low-field region, MR exhibits a SC feature with zero resistance ($R = 0$). At $T = 0.4$ K, MR shows a critical magnetic field (H_c) of 2 T. H_c decreases with increasing temperature (inset) and reaches the value of 0.6 T at 3 K. SC disappears completely above 3 K. At the high-field region, MR displays clear Shubnikov–de Haas (SdH) oscillations. The oscillations are prominent at low temperatures, diminish gradually at higher temperatures, and disappear completely above 35 K. Furthermore, these oscillations are periodic but appear to have multiple periods, indicating the existence of multiple frequencies. The frequency of these oscillations can be determined by taking the fast Fourier transform.

Figure 1(c) displays the frequency spectrum of the quantum oscillations data shown in Fig. 1(b). There are nine distinct frequency peaks at 6, 19, 83, 198, 252, 716, 841, 1500, and 2021 T. A previous MR measurement by Fu *et al.* [23] up to 32 T at ambient pressure reported four frequency peaks (27, 73, 727, and 786 T). Our frequency data, namely, 19, 83, 252, 716, and 841 T, are comparable to those reported by Fu *et al.* [23]. A slight difference in the frequency values could be attributed to the application of moderate pressure (0.22 GPa) in our experiment. It is important to note that we observed additional peaks at 1500 and 2021 T that were not detected in the previous MR experiment [23]. However, a recent MR report by Ortiz *et al.* [14] observed these high-frequency signals reaching up to 2000 T in CsV_3Sb_5, and our frequency data are comparable with their findings. In fact, our previous torque and TDO experiments [15], along with other studies [24,25,39], have reported the observation of de Haas–van Alphen oscillations with frequencies as high as 10 kT in CsV_3Sb_5.

As seen in Fig. 1(c), the amplitude of the frequency decreases at higher temperatures, which can be explained by the Lifshitz-Kosevich (LK) formula [40]. It is important to note that the higher frequencies (above 500 T) diminish faster with temperature than the lower frequencies (below 500 T). All high frequencies completely disappear above 8 K, while lower frequencies persist up to 45 K. There are several peaks, indicated by asterisks, which are not clearly defined. They quickly disappear with temperature. Such behavior of high-frequency peaks with temperature in AV_3Sb_5 has been observed in our previous torque magnetometry studies [15–17]. We have fitted the temperature-dependent frequency data for 19, 83, and 252 T using the LK fit, and the effective masses of the charge carriers are found to be $(0.107 \pm 0.006)m_o$, $(0.144 \pm 0.004)m_o$, and $(0.446 \pm 0.012)m_o$, respectively, where m_o represents the rest mass of an electron.
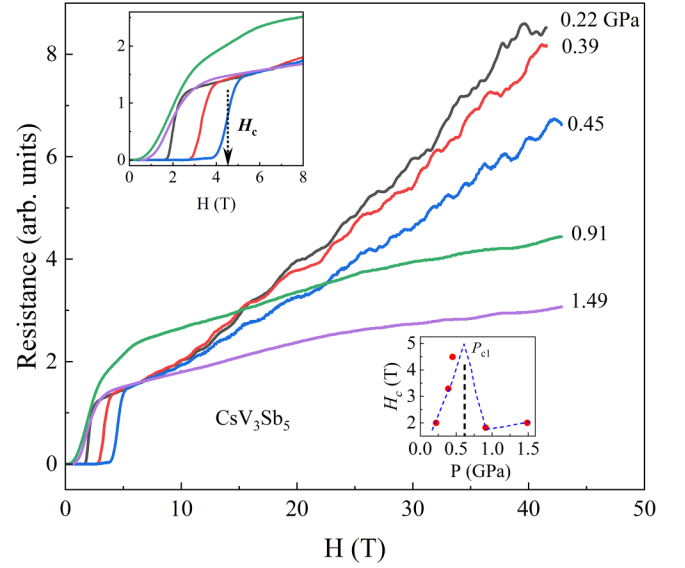

FIG. 2. Magnetoresistance (MR) curves of CsV_3Sb_5 at various pressures measured at 0.4 K. Quantum oscillations are observed at lower pressures and gradually diminish at higher-pressure values. Upper inset: Zoomed-in MR curves at low magnetic fields. Lower inset: Plot of the critical field H_c vs pressure. H_c at each pressure point is determined by taking the midpoint of the transition. The dashed curve is a guide to the eye.

To explore the pressure effect on the FS of CsV_3Sb_5, we measured its MR at five different pressure points ($P = 0.22$, 0.39, 0.45, 0.91, and 1.49 GPa), as presented in Fig. 2. The pressure points are chosen such that they lie below and above $P_{c1} \sim 0.7$ GPa. At the low-field region, the SC transition with zero resistance ($R = 0$) is clearly observed at all measured pressure values. The transition to the SC state is sharp at low pressure, which becomes broader while increasing pressure (upper inset in Fig. 2). The variation of the critical field H_c with pressure is shown in the lower inset. Initially, H_c increases with pressure, reaching its maximum value of 4.5 T at 0.45 GPa. However, it decreases with further pressure increase and then rises again after surpassing 1 GPa. Such reentrant behavior of H_c under pressure has also been observed in previous high-pressure studies [26–28] in CsV_3Sb_5. In the high-field region, MR curves show distinct SdH oscillations. As depicted in the graph, SdH oscillations are pronounced in MR curves below P_{c1}, whereas they are suppressed upon crossing P_{c1}. Additionally, both high- and low-frequency signals seem to be present below P_{c1}, while only a low-frequency signal is observed above it. This is further evident in the pressure-dependent frequency plot depicted in Fig. 3.

Figure 3 displays the temperature dependence of frequency spectra for CsV_3Sb_5 at different pressures. At $P = 0.39$ GPa, six visible peaks (13, 83, 194, 257, 745, and 1490 T) are observed. The spectrum at $P = 0.39$ GPa is comparable to that at $P = 0.22$ GPa [Fig. 1(c)]; however, there is a slight change in peak position, likely due to the pressure effect. The four low-frequency peaks are observed at all pressures, while the peak near 750 T was only observed up to 0.45 GPa, and the peak near 1500 T only up to 0.39 GPa. These observations confirm the presence of only low-frequency peaks above
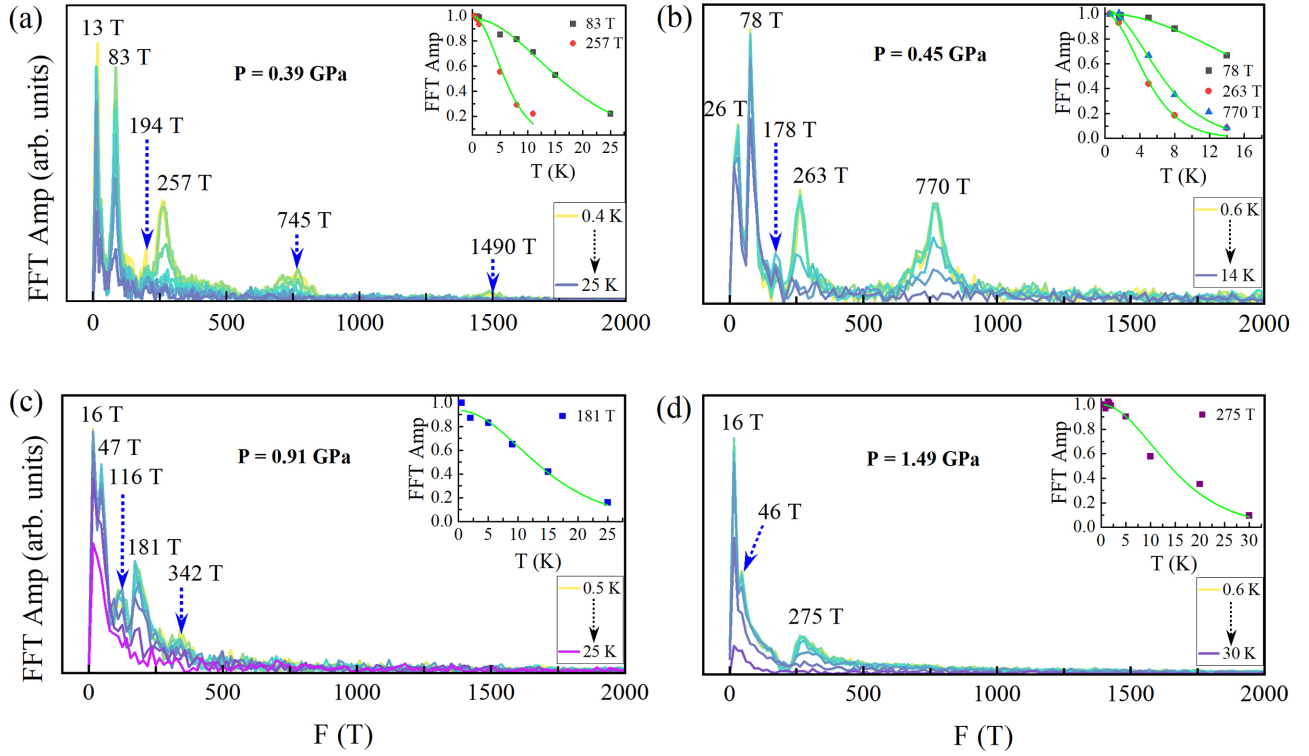
FIG. 3. The frequency spectrum of CsV_3Sb_5 at (a) 0.39, (b) 0.45, (c) 0.91, and (d) 1.49 GPa. Low-frequency signals (below 500 T) are present at all measured pressure values, while high frequencies (above 500 T) are present only below $P_{c1} \sim 0.7$ GPa. The amplitude decreases as the temperature increases. Insets: The Lifshitz-Kosevich (LK) analyses for estimating the effective mass of charge carriers.

P_{c1}, with high frequencies disappearing entirely beyond this threshold.

The LK analyses for the temperature-dependent frequency peaks are shown in the insets of Figs. 3(a)–3(d). The solid green curves are the best-fit curves to the data. The estimated effective masses of charge carriers at different pressures are presented in Table I. These mass values are comparable to those reported in previous quantum oscillation studies [14–25] on AV_3Sb_5. The effective mass computed using DFT is also

TABLE I. Effective mass (m^*) of charge carriers and Shubnikov–de Haas (SdH) oscillation frequencies under various applied pressures. The DFT-computed effective masses of the charge carriers are also included for comparison. Here, m_o represents the electron rest mass.

P (GPa)	F (T)	m^*/m_o	m^*/m_o (DFT)
	19	0.107 ± 0.006	0.186
0.22	83	0.144 ± 0.004	
	252	0.446 ± 0.012	0.437
0.39	83	0.165 ± 0.006	
	257	0.452 ± 0.022	0.449
	78	0.140 ± 0.004	
0.45	263	0.568 ± 0.025	0.471
	770	0.421 ± 0.010	
0.91	181	0.195 ± 0.012	
1.49	275	0.191 ± 0.013	

included in Table I. As shown, the experimental values and DFT-calculated masses are in close agreement.

IV. DFT CALCULATIONS

To understand the experimental observations, we computed the electronic structures of CsV_3Sb_5 under varying pressures in one of its proposed CDW phases. This compound undergoes the CDW phase transition below 94 K with the formation of superstructures. Tan *et al.* [10] have shown that the CDW phase in AV_3Sb_5 originates due to the breathing-phonon modes of the kagome lattice and is electronically mediated by the FS instability. This leads to two different superstructures in the CDW phase: the Star of David (SD) structure and the inverse Star of David (ISD) [Fig. 4(a)]. Both SD and ISD structures exhibit an in-plane 2×2 superlattice. While both CDW phases are energetically more favorable than the pristine phase, the ISD phase is preferred over the SD phase in terms of energy [10,14]. Therefore, we have considered the ISD phase for the electronic structure calculations of CsV_3Sb_5 in the present study. Furthermore, in the pressure-dependent DFT calculations, we assumed the pressure to be purely hydrostatic.

Figure 4(b) presents the electronic band structure of CsV_3Sb_5 in the ISD phase along high-symmetry points. At ambient pressure, there are multiple Dirac-like crossings near the Fermi level, as indicated by the dotted circles. The application of pressure resulted in clear changes in the band structure near the Fermi level, with a notable shift of bands being observed. The Dirac points also exhibit noticeable shifts
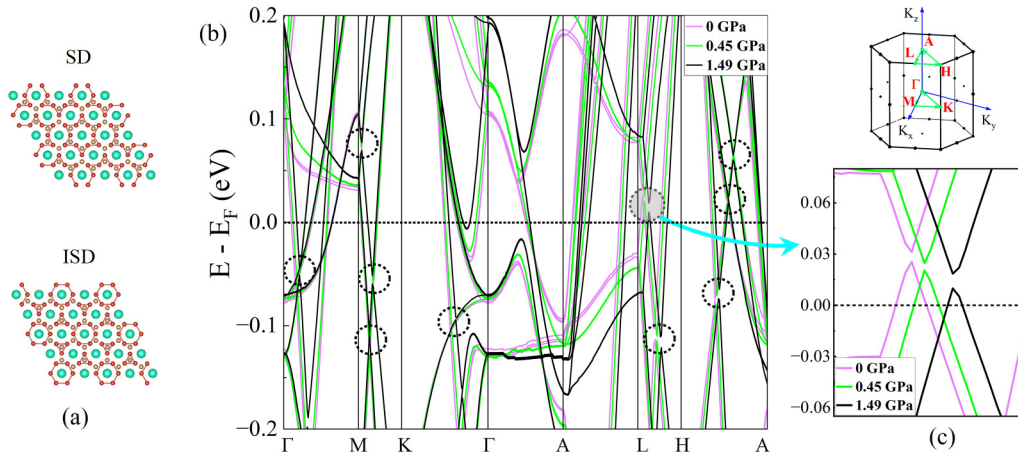
FIG. 4. (a) Star of David (SD) (top panel) and inverse Star of David (ISD) (bottom panel) CDW phases of CsV_3Sb_5. (b) Electronic band structure of CsV_3Sb_5 in the ISD phase calculated at 0, 0.45, and 1.49 GPa. The Dirac points near the Fermi level are indicated by the dotted circles. Electronic bands and Dirac crossing points shift with pressure. (c) Upper panel: Brillouin zone and high-symmetry points for CsV_3Sb_5. Lower panel: Enlarged view of the Dirac points along the *L-H* direction [highlighted region in (b)]. The Dirac point shifts to the right and moves closer to the Fermi level as the pressure increases.

with increasing pressure. The lower panel in Fig. 4(c) presents a close-up view of the electronic bands near the Fermi level along the *L-H* direction. The Dirac cone, initially located around 30 meV above the Fermi level at 0 GPa, shifts gradually to 22 and 14 meV at pressures of 0.45 and 1.49 GPa, respectively.

In the electronic band structure, each band, whether in the valence or conduction band, is identified by a number. Not all bands intersect the Fermi level; only those that do contribute to the FS. For this material, bands 265, 266, 267, 268, and 269 cross the Fermi level and thus contribute to the Fermi surface. The band-resolved FS for CsV_3Sb_5 at different pressures is shown in Fig. 5. The Fermi surface is complex. There are five pockets that have contributions from bands: 265, 266, 267, 268, and 269. The FS pocket derived from band 265 exhibits a concave shape and is located at the Brillouin zone boundaries. Similarly, the pocket from band 267 comprises three pieces: concavelike structures at the top and bottom of the Brillouin zone and a nearly spherical pocket at the center. As pressure increases, the concavelike structures enlarge, while the spherical pocket undergoes significant shrinkage. A similar trend is observed for the FS of band 268, with the exception that the central spherical pocket shrinks and eventually disappears completely at a pressure of 1.49 GPa. The pockets from bands 265 and 266 also exhibit dimensional changes under pressure, although not as prominently as those from bands 267, 268, and 269. These observations confirm that the FS of CsV_3Sb_5 is highly sensitive to the application of external pressure.

To compare with experimental data, we measured the area of each energy isosurface forming the FS and then computed the oscillatory frequencies using the Onsager relation [42]. We utilized the SKEAF code [43] to compute all possible frequencies from each FS pocket. The calculated frequencies at different pressures, together with experimental data, are shown in Fig. 6. The high-frequency signals around 1000 and 1600 T correspond to the FS pocket of band 266, while the low-frequency signals below 500 T originate from FS pockets of bands 265, 267, 268, and 269. As seen in the graph,

the frequencies calculated from DFT are nearly comparable with the experimental values. However, DFT results do not describe the absence of high frequencies (above 500 T) above P_{c1}. One of the possible reasons could be that the sample inside the pressure cell is slightly misaligned with respect to the magnetic fields by a few degrees. To rule out this possibility, we examined how the frequency value varies when adjusting the tilt angle by a few degrees in both the polar and azimuthal directions, but the frequencies show no significant change (Fig. S3 in the SM [35]). This does not account for the absence of high-frequency signals above P_{c1}. Another possibility could be that the DFT calculations are conducted by considering a $2 \times 2 \times 1$ ISD structure in the CDW phase, which may not represent the real ground state. Several computational studies [44,45] have adjusted the Fermi energy to match experimental quantum oscillation data, assuming ambiguity in the experimental Fermi energy. We observed that shifting the Fermi level alters the shape and size of the FS and, consequently, the frequencies, as shown in Fig. S4 in the SM [35]. Upward and downward shifts in the Fermi level yield different frequency values. Therefore, we did not conduct detailed calculations for frequency shifts until it is clearly known in which direction and by how much the Fermi energy should be adjusted.

Recently, Tan *et al.* [41] conducted comprehensive computational studies to explain the experimentally observed quantum oscillation frequencies in CsV_3Sb_5. Their results indicate that although some of the experimental frequencies can be explained using $2 \times 2 \times 1$ (SD or ISD) CDW structures, a better match is achieved with a $2 \times 2 \times 2$ CDW phase with interlayer structural modulation. Performing DFT calculations with a $2 \times 2 \times 2$ CDW structure is beyond our computational resources at this moment.

V. DISCUSSION AND CONCLUSION

Here, we have explored the fermiology of CsV_3Sb_5 at different pressures by measuring Shubnikov–de Haas (SdH)
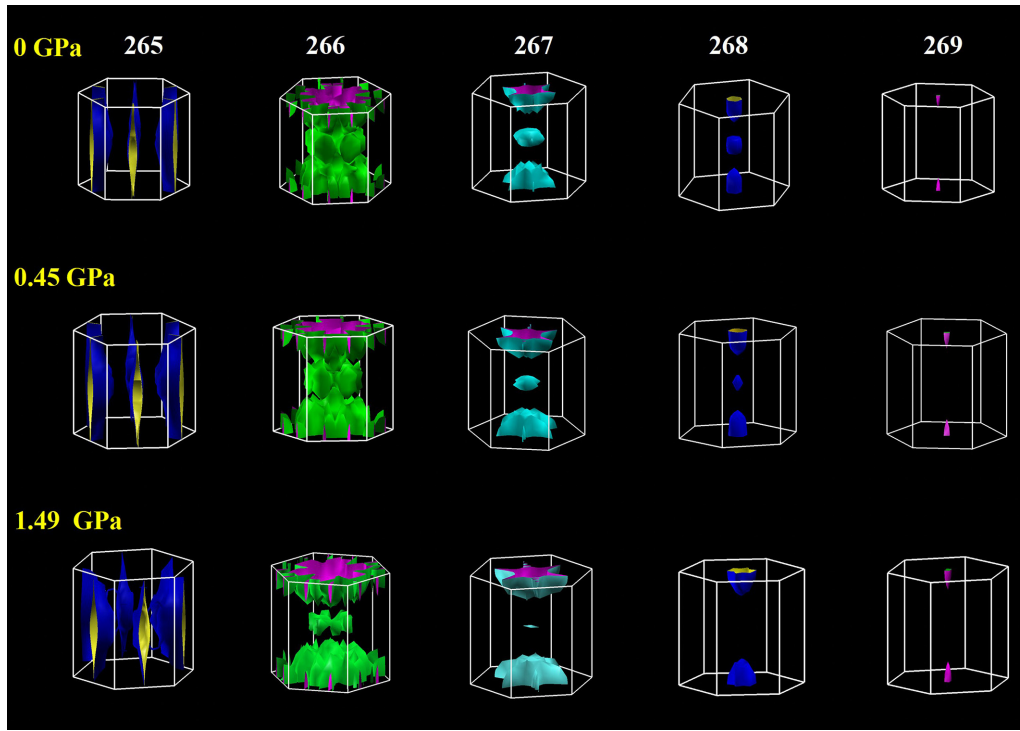
FIG. 5. Band-resolved Fermi surface (FS) of CsV_3Sb_5 in the CDW (ISD) state computed at various pressures. The FS consists of contributions from five pockets, corresponding to bands 265, 266, 267, 268, and 269. The size and shape of the FS pockets evolve as pressure increases.

oscillations. The magnetoresistance (MR) measured up to 43 T exhibits distinct SdH oscillations with multiple frequencies, reaching up to 2000 T. Notably, the high-frequency signals (above 500 T) vanish as pressure increases beyond $P_{c1} \sim 0.7$ GPa. According to Onsager's relation [40,46–48],
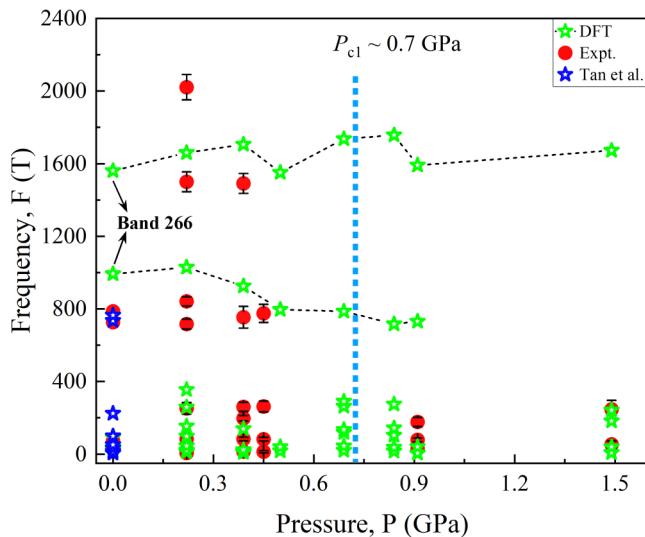

FIG. 6. Pressure dependence of SdH frequencies for CsV_3Sb_5. The solid red circles are experimental data, whereas the green stars are possible frequencies calculated using DFT. High frequencies ~1000 and 1600 T arise from the Fermi surface of band 266. The vertical line is a guide for P_{c1}. The blue stars are data from Tan *et al.* [41].

the frequency (F) of quantum oscillations is directly proportional to the cross-sectional area (A_F) of the FS as $F = \hbar/(2\pi e)A_F^2$, where $\hbar$ is the reduced Planck's constant and e is the charge of an electron. Therefore, the quantum oscillation frequency is the direct measure of the FS of the material under study. The absence of a high-frequency signal above P_{c1} in this study strongly suggests that the FS undergoes a reconstruction above P_{c1}. One might wonder why the frequencies near 750 and 1500 T do not simultaneously vanish as the pressure increases from $P = 0.39$ to 0.45 GPa [Figs. 3(a) and 3(b)]. These frequencies arise from different cross sections of a single FS pocket or possibly from two distinct FS pockets. Our experimental data suggest that as the pressure increases, the FS cross section contributing to the 750 T frequency remains largely unchanged, whereas the one corresponding to the 1500 T frequency undergoes significant deformation. This pressure-induced FS instability might have led to both the change in SC behavior [26,27] with the sharp change in T_c and the emergence of a new stripelike CDW feature in a high-pressure NMR experiment [28] at P_{c1}.

To interpret the experimental observations, we performed pressure-dependent electronic structure calculations of CsV_3Sb_5 using density functional theory (DFT). The electronic bands and Fermi surface (FS) calculated in one of the proposed charge density wave (CDW) phases, the 2 × 2 × 1 inverse Star of David (ISD) phase, show clear band shifts and changes in the shape of the Fermi surfaces under moderate pressure, up to 1.5 GPa. However, in contrast to our experimental results, the DFT-calculated frequencies persist even beyond $P_{c1} \sim 0.7$ GPa. This suggests that the CDW phase in CsV_3Sb_5 is likely three dimensional in nature,

and pressure-dependent DFT calculations incorporating inter-layer coupling, particularly in the $2 \times 2 \times 2$ and $2 \times 2 \times 4$ phases, may be required to fully explain the experimental findings.

There might be a question that the change in SdH oscillation could be due to the pressure inhomogeneity or nonhydrostaticity. Here, we have used Daphne 7474 oil as a pressure-transmitting medium. The hydrostatic limit, where the liquid solidifies, at room temperature for this fluid is between 3 and 4 GPa [49], far above the maximum pressure that we applied (1.49 GPa) in the present research. Furthermore, the pressure medium becomes solid with cooling, but the hydrostaticity can be estimated by the full width at half maximum (FWHM) of a ruby peak inside the medium. It has been found that Daphne 7474 remains hydrostatic (the peak does not broaden) down to 77 K [50]. Therefore, it is unlikely that pressure inhomogeneity or nonhydrostatic conditions could have caused the change in SdH oscillations above P_{c1}; instead, it is solely caused by FS reconstruction.

The tuning of the FS can also be done by doping, where the doping element acts as chemical pressure. There are several studies [29–32,51] on the tuning of electronic properties in AV$_3$Sb$_5$ through doping. For example, Hou *et al.* [32] have studied the evolution of CDW and SC properties with Ti doping in CsV$_{(3-x)}$Ti$_x$Sb$_5$. They also observed the double-dome SC, similar to the high-pressure studies [26–28]. Although chemical doping is a crucial method for tuning electronic properties, it often introduces impurities and defects, ulti-mately reducing the single-crystal quality [51] in AV$_3$Sb$_5$, making the study of their intrinsic properties challenging. Instead, high pressure is a clean method to tune electronic properties without introducing extrinsic artifacts. Therefore, the detailed high-pressure studies presented under high magnetic fields in this work will be crucial to shed light on the double-dome SC feature and CDW phase in AV$_3$Sb$_5$ and other vanadium-based kagome compounds.

[1] S. D. Wilson and B. R. Ortiz, AV$_3$Sb$_5$ kagome superconductors, Nat. Rev. Mater. **9**, 420 (2024).

[2] L. Ye, M. Kang, J. Liu, F. von Cube, C. R. Wicker, T. Suzuki, C. Jozwiak, A. Bostwick, E. Rotenberg, D. C. Bell, L. Fu, R. Comin, and J. G. Checkelsky, Massive Dirac fermions in a ferromagnetic kagome metal, Nature (London) **555**, 638 (2018).

[3] J.-X. Yin, W. Ma, T. A. Cochran, X. Xu, S. S. Zhang, H.-J. Tien, N. Shumiya, G. Cheng, K. Jiang, B. Lian *et al.*, Quantum-limit Chern topological magnetism in tbmn6sn6, Nature (London) **583**, 533 (2020).

[4] K. Jiang, T. Wu, J.-X. Yin, Z. Wang, M. Z. Hasan, S. D. Wilson, X. Chen, and J. Hu, Kagome superconductors AV$_3$Sb$_5$ (A = K, Rb, Cs), Natl. Sci. Rev. **10**, nwac199 (2022).

[5] B. R. Ortiz, L. C. Gomes, J. R. Morey, M. Winiarski, M. Bordelon, J. S. Mangum, I. W. H. Oswald, J. A. Rodriguez-Rivera, J. R. Neilson, S. D. Wilson, E. Ertekin, T. M. McQueen, and E. S. Toberer, New kagome prototype materials: Discovery of KV$_3$Sb$_5$, RbV$_3$Sb$_5$, and CsV$_3$Sb$_5$, Phys. Rev. Mater. **3**, 094407 (2019).

[6] B. R. Ortiz, P. M. Sarte, E. M. Kenney, M. J. Graf, S. M. L. Teicher, R. Seshadri, and S. D. Wilson, Superconductivity in the $\mathbb{z}_2$ kagome metal KV$_3$Sb$_5$, Phys. Rev. Mater. **5**, 034801 (2021).

[7] B. R. Ortiz, S. M. L. Teicher, Y. Hu, J. L. Zuo, P. M. Sarte, E. C. Schueller, A. M. M. Abeykoon, M. J. Krogstad, S. Rosenkranz, R. Osborn, R. Seshadri, L. Balents, J. He, and S. D. Wilson, CsV$_3$Sb$_5$: A $\mathbb{z}_2$ topological kagome metal with a superconducting ground state, Phys. Rev. Lett. **125**, 247002 (2020).

[8] N. N. Wang, K. Y. Chen, Q. W. Yin, Y. N. N. Ma, B. Y. Pan, X. Yang, X. Y. Ji, S. L. Wu, P. F. Shan, S. X. Xu, Z. J. Tu, C. S. Gong, G. T. Liu, G. Li, Y. Uwatoko, X. L. Dong, H. C. Lei, J. P. Sun, and J.-G. Cheng, Competition between charge-density-wave and superconductivity in the kagome metal RbV$_3$Sb$_5$, Phys. Rev. Res. **3**, 043018 (2021).

[9] M. Kang, S. Fang, J.-K. Kim, B. R. Ortiz, S. H. Ryu, J. Kim, J. Yoo, G. Sangiovanni, D. Di Sante, B.-G. Park *et al.*, Twofold van Hove singularity and origin of charge order in topological kagome superconductor CsV$_3$Sb$_5$, Nat. Phys. **18**, 301 (2022).

[10] H. Tan, Y. Liu, Z. Wang, and B. Yan, Charge density waves and electronic properties of superconducting kagome metals, Phys. Rev. Lett. **127**, 046401 (2021).

[11] Z. Liang, X. Hou, F. Zhang, W. Ma, P. Wu, Z. Zhang, F. Yu, J.-J. Ying, K. Jiang, L. Shan, Z. Wang, and X.-H. Chen, Three-dimensional charge density wave and surface-dependent vortex-core states in a kagome superconductor CsV$_3$Sb$_5$, Phys. Rev. X **11**, 031026 (2021).

[12] J. Frassineti, P. Bonfà, G. Allodi, E. Garcia, R. Cong, B. R. Ortiz, S. D. Wilson, R. De Renzi, V. F. Mitrović, and S. Sanna, Microscopic nature of the charge-density wave in the kagome superconductor RbV$_3$Sb$_5$, Phys. Rev. Res. **5**, L012017 (2023).

[13] Q. Wang, P. Kong, W. Shi, C. Pei, C. Wen, L. Gao, Y. Zhao, Q. Yin, Y. Wu, G. Li *et al.*, Charge density wave orders and enhanced superconductivity under pressure in the kagome metal csv3sb5, Adv. Mater. **33**, 2102813 (2021).

[14] B. R. Ortiz, S. M. L. Teicher, L. Kautzsch, P. M. Sarte, N. Ratcliff, J. Harter, J. P. C. Ruff, R. Seshadri, and S. D. Wilson,

Fermi surface mapping and the nature of charge-density-wave order in the kagome superconductor CsV_3Sb_5, Phys. Rev. X **11**, 041030 (2021).

[15] K. Shrestha, R. Chapai, B. K. Pokharel, D. Miertschin, T. Nguyen, X. Zhou, D. Y. Chung, M. G. Kanatzidis, J. F. Mitchell, U. Welp, D. Popović, D. E. Graf, B. Lorenz, and W. K. Kwok, Nontrivial fermi surface topology of the kagome superconductor CsV_3Sb_5 probed by de Haas–van Alphen oscillations, Phys. Rev. B **105**, 024508 (2022).

[16] K. Shrestha, M. Shi, T. Nguyen, D. Miertschin, K. Fan, L. Deng, D. E. Graf, X. Chen, and C.-W. Chu, Fermi surface mapping of the kagome superconductor RbV_3Sb_5 using de Haas–van Alphen oscillations, Phys. Rev. B **107**, 075120 (2023).

[17] K. Shrestha, M. Shi, B. Regmi, T. Nguyen, D. Miertschin, K. Fan, L. Z. Deng, N. Aryal, S.-G. Kim, D. E. Graf, X. Chen, and C. W. Chu, High quantum oscillation frequencies and nontrivial topology in kagome superconductor KV_3Sb_5 probed by torque magnetometry up to 45 T, Phys. Rev. B **107**, 155128 (2023).

[18] F. H. Yu, T. Wu, Z. Y. Wang, B. Lei, W. Z. Zhuo, J. J. Ying, and X. H. Chen, Concurrence of anomalous Hall effect and charge density wave in a superconducting topological kagome metal, Phys. Rev. B **104**, L041103 (2021).

[19] Q. Yin, Z. Tu, C. Gong, Y. Fu, S. Yan, and H. Lei, Superconductivity and normal-state properties of kagome metal RbV_3Sb_5 single crystals, Chin. Phys. Lett. **38**, 037403 (2021).

[20] S.-Y. Yang, Y. Wang, B. R. Ortiz, D. Liu, J. Gayles, E. Derunova, R. Gonzalez-Hernandez, L. Šmejkal, Y. Chen, S. S. Parkin *et al.*, Giant, unconventional anomalous Hall effect in the metallic frustrated magnet candidate, KV_3Sb_5, Sci. Adv. **6**, eabb6003 (2020).

[21] K. Nakayama, Y. Li, T. Kato, M. Liu, Z. Wang, T. Takahashi, Y. Yao, and T. Sato, Carrier injection and manipulation of charge-density wave in kagome superconductor CsV_3Sb_5, Phys. Rev. X **12**, 011001 (2022).

[22] H. Luo, Q. Gao, H. Liu, Y. Gu, D. Wu, C. Yi, J. Jia, S. Wu, X. Luo, Y. Xu *et al.*, Electronic nature of charge density wave and electron-phonon coupling in kagome superconductor KV_3Sb_5, Nat. Commun. **13**, 273 (2022).

[23] Y. Fu, N. Zhao, Z. Chen, Q. Yin, Z. Tu, C. Gong, C. Xi, X. Zhu, Y. Sun, K. Liu, and H. Lei, Quantum transport evidence of topological band structures of kagome superconductor CsV_3Sb_5, Phys. Rev. Lett. **127**, 207002 (2021).

[24] W. Zhang, L. Wang, C. W. Tsang, X. Liu, J. Xie, W. C. Yu, K. T. Lai, and S. K. Goh, Emergence of large quantum oscillation frequencies in thin flakes of the kagome superconductor CsV_3Sb_5, Phys. Rev. B **106**, 195103 (2022).

[25] C. Broyles, D. Graf, H. Yang, X. Dong, H. Gao, and S. Ran, Effect of the interlayer ordering on the fermi surface of kagome superconductor CsV_3Sb_5 revealed by quantum oscillations, Phys. Rev. Lett. **129**, 157001 (2022).

[26] K. Y. Chen, N. N. Wang, Q. W. Yin, Y. H. Gu, K. Jiang, Z. J. Tu, C. S. Gong, Y. Uwatoko, J. P. Sun, H. C. Lei, J. P. Hu, and J.-G. Cheng, Double superconducting dome and triple enhancement of T_c in the kagome superconductor csv_3sb_5 under high pressure, Phys. Rev. Lett. **126**, 247001 (2021).

[27] F. Yu, D. Ma, W. Zhuo, S. Liu, X. Wen, B. Lei, J. Ying, and X. Chen, Unusual competition of superconductivity and charge-density-wave state in a compressed topological kagome metal, Nat. Commun. **12**, 3645 (2021).

[28] L. Zheng, Z. Wu, Y. Yang, L. Nie, M. Shan, K. Sun, D. Song, F. Yu, J. Li, D. Zhao *et al.*, Emergent charge order in pressurized kagome superconductor CsV_3Sb_5, Nature (London) **611**, 682 (2022).

[29] Y. M. Oey, B. R. Ortiz, F. Kaboudvand, J. Frassineti, E. Garcia, R. Cong, S. Sanna, V. F. Mitrović, R. Seshadri, and S. D. Wilson, Fermi level tuning and double-dome superconductivity in the kagome metal $CsV_3Sb_{5-x}Sn_x$, Phys. Rev. Mater. **6**, L041801 (2022).

[30] A. N. Capa Salinas, B. R. Ortiz, C. Bales, J. Frassineti, V. F. Mitrović, and S. D. Wilson, Electron-hole asymmetry in the phase diagram of carrier-tuned CsV_3Sb_5, Frontiers Electron. Mater. **3**, 1257490 (2023).

[31] H. Yang, Z. Huang, Y. Zhang, Z. Zhao, J. Shi, H. Luo, L. Zhao, G. Qian, H. Tan, B. Hu *et al.*, Titanium doped kagome superconductor $CsV_{3-x}Ti_xSb_5$ and two distinct phases, Sci. Bull. **67**, 2176 (2022).

[32] J. Hou, K. Y. Chen, J. P. Sun, Z. Zhao, Y. H. Zhang, P. F. Shan, N. N. Wang, H. Zhang, K. Zhu, Y. Uwatoko, H. Chen, H. T. Yang, X. L. Dong, H.-J. Gao, and J.-G. Cheng, Effect of hydrostatic pressure on the unconventional charge density wave and superconducting properties in two distinct phases of doped kagome superconductors $CsV_{3-x}Ti_xSb_5$, Phys. Rev. B **107**, 144502 (2023).

[33] A. A. Tsirlin, B. R. Ortiz, M. Dressel, S. D. Wilson, S. Winnerl, and E. Uykur, Effect of nonhydrostatic pressure on the superconducting kagome metal CsV_3Sb_5, Phys. Rev. B **107**, 174107 (2023).

[34] A. Tsirlin, P. Fertey, B. R. Ortiz, B. Klis, V. Merkl, M. Dressel, S. Wilson, and E. Uykur, Role of Sb in the superconducting kagome metal CsV_3Sb_5 revealed by its anisotropic compression, SciPost Phys. **12**, 049 (2022).

[35] See Supplemental Material at http://link.aps.org/supplemental/10.1103/PhysRevB.110.205135 for detailed information on the temperature dependence of resistivity, magnetic susceptibility, angle- and Fermi-level-dependent quantum oscillation frequencies, etc.

[36] P. Giannozzi, S. Baroni, N. Bonini, M. Calandra, R. Car, C. Cavazzoni, D. Ceresoli, G. L. Chiarotti, M. Cococcioni, I. Dabo *et al.*, QUANTUM ESPRESSO: A modular and open-source software project for quantum simulations of materials, J. Phys.: Condens. Matter **21**, 395502 (2009).

[37] P. Blaha, K. Schwarz, G. K. Madsen, D. Kvasnicka, J. Luitz *et al.*, *An Augmented Plane Wave+ Local Orbitals Program for Calculating Crystal Properties*, Vol. 60 (Techn. Universitat., 2001).

[38] J. P. Perdew, K. Burke, and M. Ernzerhof, Generalized gradient approximation made simple, Phys. Rev. Lett. **77**, 3865 (1996).

[39] R. Chapai, M. Leroux, V. Oliviero, D. Vignolles, N. Bruyant, M. P. Smylie, D. Y. Chung, M. G. Kanatzidis, W.-K. Kwok, J. F. Mitchell, and U. Welp, Magnetic breakdown and topology in the kagome superconductor CsV_3Sb_5 under high magnetic field, Phys. Rev. Lett. **130**, 126401 (2023).

[40] D. Shoenberg, *Magnetic Oscillations in Metals* (Cambridge University Press, Cambridge, 1984).

[41] H. Tan, Y. Li, Y. Liu, D. Kaplan, Z. Wang, and B. Yan, npj Quantum Mater. **8**, 39 (2023).

[42] According to the Onsager's relation, the quantum oscillation measured frequency of an electron orbit (F) which is perpen-

dicular to the applied magnetic field is related to the area of the Fermi surface (A) by $F = \frac{\phi_0}{2\pi^2}A$, where $\phi_0 = 2.07 \times 10^{-15}$ T.m^2 is the quantum of flux.

[43] S. Julian, Numerical extraction of de Haas–van Alphen frequencies from calculated band energies, Comput. Phys. Commun. **183**, 324 (2012).

[44] W. Zheng, R. Schönemann, S. Mozaffari, Y.-C. Chiu, Z. B. Goraum, N. Aryal, E. Manousakis, T. M. Siegrist, K. Wei, and L. Balicas, Bulk Fermi surfaces of the Dirac type-II semimetallic candidate NiTe$_2$, Phys. Rev. B **102**, 125103 (2020).

[45] T. Nguyen, N. Aryal, B. K. Pokharel, L. Harnagea, D. Mierstchin, D. Popović, D. E. Graf, and K. Shrestha, Fermiology of the Dirac type-II semimetal candidates (Ni, Zr)Te$_2$ using de Haas–van Alphen oscillations, Phys. Rev. B **106**, 075154 (2022).

[46] Y. Ando, Topological insulator materials, J. Phys. Soc. Jpn. **82**, 102001 (2013).

[47] K. Shrestha, V. Marinova, B. Lorenz, and P. C. W. Chu, Shubnikov–de Haas oscillations from topological surface states of metallic Bi$_2$Se$_{2.1}$Te$_{0.9}$, Phys. Rev. B **90**, 241111(R) (2014).

[48] K. Shrestha, V. Marinova, B. Lorenz, and C. Chu, Evidence of a 2D Fermi surface due to surface states in a p-type metallic Bi$_2$Te$_3$, J. Phys.: Condens. Matter **30**, 185601 (2018).

[49] K. Murata, K. Yokogawa, H. Yoshino, S. Klotz, P. Munsch, A. Irizawa, M. Nishiyama, K. Iizuka, T. Nanba, T. Okada *et al.*, Pressure transmitting medium daphne 7474 solidifying at 3.7 GPa at room temperature, Rev. Sci. Instrum. **79**, 085101 (2008).

[50] N. Tateiwa and Y. Haga, Evaluations of pressure-transmitting media for cryogenic experiments with diamond anvil cell, Rev. Sci. Instrum. **80**, 123901 (2009).

[51] F. Song, Y. Liu, H. Ni, Y. Chen, C. Cheng, and Y. Zhao, Growth and superconductivity of the kagome metal CsV$_3$(Sb$_{1-x}$Se$_x$)$_5$ single crystals, Phys. Lett. A **510**, 129526 (2024).